Available online at www.sciencedirect.com

SCIENCE DIRECT

Cement and Concrete Research 35 (2005) 597–608

CEMENT AND CONCRETE RESEARCH

Numerical modeling of transport phenomena in reinforced concrete exposed to elevated temperatures

Jae H. Chung*, Gary R. Consolazio

Department of Civil and Coastal Engineering, University of Florida, P.O. Box 116580, Gainesville, FL 32611, USA

Received 18 December 2003; accepted 24 May 2004

Abstract

The objective of this study is to develop a finite difference model that simulates coupled heat and mass transport phenomena in reinforced concrete structures exposed to rapid heating conditions such as fires. A mathematical and computational model for simulating the multidimensional, thermohydrological response of reinforced concrete structural elements is developed and subsequently used to study the effects of steel reinforcement on thermodynamic state variables. Key material parameters describing multiphase fluid flow and thermohydrological behavior of concrete are discussed. Spatial and temporal distributions of temperature, pore pressure, and degree of saturation are illustrated as predicted under extreme thermal-loading conditions. Simulation results indicate that the presence of steel reinforcement impedes moisture movement and produces quasi-saturated zones in cover concrete where significant pore pressures are developed.

Keywords: Temperature; Thermal analysis; Transport properties; High-performance concrete; Spalling

1. Introduction

In regard to the potential influence of pore pressures on thermal spalling, the low permeability of high-strength concrete (HSC) has been suspected to limit moisture movement in heated concrete elements and result in the development of severe internal pore pressures [1–3]. In addition, material properties such as strength and modulus of elasticity [4] and mechanical responses such as stress and strain development [5] are significantly influenced by the thermodynamic state—as characterized by variables such as pore pressure, temperature, and saturation—of reinforced concrete structures. Violent material failure (i.e., explosive spalling) of low-permeability concrete has also been reported in field and laboratory tests [3,6]. In these tests, large areas of steel reinforcement were exposed to direct thermal loading by spalling of the concrete cover after 10–25 min of fire exposure. Previous studies [1,7] have shown that under sustained thermal loading, internal pore pressures developed as a result of thermally induced moisture clog formation can be quite substantial.

However, the influence of steel reinforcement on thermohydrological behavior of near-surface concrete, i.e., cover concrete normally expected to thermally protect internal reinforcing steel, has not received adequate quantitative study in the past. In this paper, it will be demonstrated that the presence of reinforcing steel bars in composite reinforced concrete (R/C) members influences moisture movement during thermal loading and can significantly alter the development of thermodynamic state variables, particularly internal pore pressure. Steel reinforcing bars can create impermeable regions that impede the migration of moisture and force flow to occur through the concrete matrix surrounding the bars. A goal of this paper is to numerically quantify such effects and to evaluate their influence on thermal spalling of R/C structures subjected to rapid heating.

To accomplish this goal, a computational model for simulating three-dimensional (3-D) coupled fluid and heat transport in R/C members is developed. Formulating mathematical representations of key physical phenomena is a primary component of the model development process presented here. The TOUGH2 simulation code [8], a gen-

* Corresponding author. Tel.: +1-352-392-9537x1511; fax: +1-352-392-3394.
E-mail addresses: jchun@ce.ufl.edu (J.H. Chung), grc@ce.ufl.edu (G.R. Consolazio).

0008-8846/$ – see front matter © 2004 Elsevier Ltd. All rights reserved.
doi:10.1016/j.cemconres.2004.05.037

eral-purpose, finite-difference numerical simulator for multiphase fluid and heat flow, forms the basis of the model. The mathematical formulation implemented in TOUGH2 consists of transient mass and thermal energy balance equations that are used to transiently solve for three primary variables: pore pressure, degree of gas saturation, and temperature.

Newly developed constitutive relationships, including key fluid flow material parameters for low-permeability concrete, are implemented in the numerical model described here. Modifications are then made to the TOUGH2 code so that flow characteristics specific to near-surface concrete behavior are properly taken into consideration. For example, *relative permeability functions* and *slip–flow relationships* are developed specifically for cement-based materials and are implemented within TOUGH2. Implementation of the new features is necessary to properly describe the flow of the various fluid phases that migrate inside heated concrete. The proposed model is capable of accounting for the simultaneous movement of both gaseous and liquid fluid phases, their transport of heat, and phase transitions between liquid water and gaseous water vapor.

2. Governing equations for concrete

In the present context, concrete is assumed to consist of three phases: solid (s), liquid water (w), and gaseous (g). The balance laws used here are analogous to those of a simple continuum, except that global balances apply to the multiphase mixture as a whole via an averaging process. This averaging process is used as the framework for constructing mathematical formulations of governing field equations at the *macroscopic* level where macroscopic field variables dictate the state of the system. By using spatial averaging processes, macroscopic variables corresponding to real, laboratory-measurable quantities are used to develop appropriate governing equations.

2.1. Mass balance law for the fluid phases

Similar to the mass balance for a single fluid phase, the mass balance law for multiple fluid phases π, where $\pi = \mathrm{w}$ (liquid water) or $\pi = \mathrm{g}$ (gas), may be written [9]:

$$\frac{\partial (nS_\pi \rho^\pi)}{\partial t} + \mathrm{div}[nS_\pi \rho^\pi v^\pi] = \dot{m} \tag{1}$$

where $nS_\pi\rho^\pi$ is the macroscopic volume-averaged mass density of fluid phase π, v^π is the velocity, and $\dot{m}$ is the rate of change in mass of the fluid phases. Physically, the first term on the left side accounts for the accumulation of phase π and is known as the mass concentration of the fluid phase, the second term models the advection of phase π at the mean macroscopic flow velocity of the fluid phase, and the right-hand side of the equation accounts for the quantity of vapor gained or lost, per unit time per unit volume, through condensation or evaporation.

2.2. Energy balance equation for concrete

Assuming that a local thermodynamic equilibrium exists, the macroscopic energy balance equation used to model concrete at high temperature is written as [9]:

$$(\rho C_\mathrm{p})_\mathrm{eff} \frac{\partial T}{\partial t} + (\eta^\mathrm{w}\rho^\mathrm{w}C_\mathrm{p}^\mathrm{w}v^\mathrm{w} + \eta^\mathrm{g}\rho^\mathrm{g}C_\mathrm{p}^\mathrm{g}v^\mathrm{g}) \times \mathrm{grad}\ T$$

$$-\mathrm{div}(\kappa_\mathrm{eff}\ \mathrm{grad}\ T) + \dot{m}\Delta H_\mathrm{vapor} = 0 \tag{2}$$

where the effective heat capacity of concrete $(\rho C_\mathrm{p})_\mathrm{eff}$ is defined as: $(\rho C_\mathrm{p})_\mathrm{eff} = \eta^\mathrm{s}\rho^\mathrm{s}C_\mathrm{p}^\mathrm{s} + \eta^\mathrm{w}\rho^\mathrm{w}C_\mathrm{p}^\mathrm{w} + \eta^\mathrm{g}\rho^\mathrm{g}C_\mathrm{p}^\mathrm{g}$, in which η^π is the volume fraction of phase π and C_p^π represents the specific heat of phase π per unit mass at constant pressure, T is the absolute temperature, κ_eff is the effective heat conductivity, and ΔH_vapor is the latent heat exchange between the fluid phases in evaporation. Physical interpretation of the terms of Eq. (2) are as follows: the first term on the left represents the rate change of heat stored in the concrete; the second term accounts for heat convection by fluid flow; the third term represents the internal heat flux by conduction, and the last term on the left-hand side represents the enthalpy change due to phase transition (e.g., evaporation) of the pore moisture.

In particular, heat convection via multiphase fluid flow and thermal energy consumption associated with evaporation should be considered in the prediction of temperature profiles in the heated concrete system. Because temperature rise and thermal gradient development resulting from the solution of Eq. (2) are strongly coupled to fluid flow by the advection term in Eq. (1), the moisture movement and evaporation processes involved in temperature change are important physical phenomena. Consequently, the coupling between mass and heat transfer influences the development of thermally induced stresses in concrete structures subjected to fire [5].

3. Key parameters of fluid and heat flow in concrete

In the following, the multiphase characteristics of concrete are described using constitutive relationships between fluxes and driving forces in the mass and energy balance equations. Concrete permeabilities are expressed as intrinsic permeabilities (also called absolute permeabilities) for use in the numerical models described later. Although numerous past experimental studies have focused on the measurement of concrete permeability to either gas or liquid flow [10–14], only a very limited number of studies [15–17] have involved simultaneous experimental determination

of both liquid and gas permeabilities for identical concrete mixtures.

Results from studies of the latter type are used here to construct multiphase constitutive flow relationships for concrete. Particular attention is given to using data solely from studies using comparable sample preparation procedures (specimen casting, curing method, curing duration, etc.) because such procedures influence both intrinsic gas permeability and effective permeability in the presence of pore water content [13,18,19]. Also, only similar mixture compositions, characterized, e.g., by water to cement plus pozzolanic material ratio, i.e., W/(C + P), and aggregate to cement plus pozzolanic material ratio, i.e., Agg/(C + P), were included in the data collection process. Although the material parameters used in this study cannot possibly characterize all possible types of concrete, they are representative of typical normal-weight, normal-strength concrete (NSC) and HSC mixtures often found in practice.

3.1. Mass flow law

Application of the momentum balance principle to the flow of a single fluid phase flowing through concrete yields Darcy's law, the fundamental field equation for porous-media flow:

$$\eta^{\pi} v^{\pi} = -\frac{K}{\mu^{\pi}} (\nabla p_{\pi}) \tag{3}$$

where μ is the dynamic viscosity and K is the intrinsic permeability. In Eq. (3), the parameter K is the permeability of the porous solid matrix after normalizing for the effects of fluid viscosity and density. The goal in formulating this type of parameter, which is called the intrinsic permeability, is to arrive at a property that is intrinsic to the solid matrix and independent of specific fluid characteristics. However, even after normalizing for viscosity and density effects, experimental test data reveal considerable discrepancies between the intrinsic permeability of concrete to gas flow and liquid flow.

In particular, significant deviation from Darcy's law has been observed in tests involving gas flow through concrete. In these cases, measured flow rates exceed the rates predicted by Eq. (3). Whereas Darcy's law, which linearly relates flow velocity to pressure gradient, is well suited to modeling laminar *liquid* flow through porous materials such as soil, it is not capable of accurately modeling *gas* flow through low-porosity, low-permeability materials such as concrete. Contrary to laminar flow theory, in which zero fluid velocity is assumed at the solid–fluid interface, gas flow involves particle motion (nonzero flow velocity) even at the interface between the gas and the solid. Because of this gas "slippage," the rate of mass flow through the material exceeds that predicted either microscopically within the flow channels from Poiseuille's law or macroscopically from Darcy's law. Instead, the effect of gas *slip flow* may be mathematically approximated as [20]:

$$\eta^{g} v^{g} = -\frac{K_g}{\mu^{g}} \left(1 + \frac{b}{p_g}\right) (\nabla p_g) \tag{4}$$

where K in Eq. (3) is replaced by the intrinsic permeability to gas K_g multiplied by a slip-modification factor $(1 + b/p_g)$, b is called the slip flow constant (or the Klinkenberg constant), and p_g is the gas pressure.

In situations involving mass transport through very low permeability materials, such as HSC, the slip flow phenomenon may dominate. As Eq. (4) indicates, the effective permeability of concrete to gas flow at pressure of p_g, i.e., the quantity $K_g(1 + b/p_g)$, can be much larger than the intrinsic gas permeability K_g if the material constant b is large. A functional relationship between b and K_g has been developed [9] for cement-based materials. This relationship is illustrated in Fig. 1 and is given by the expression:

$$b = e^{(-0.5818 \ln(Kg) - 19.1213)} \tag{5}$$

where K_g is in units of square meters and b is in units of atmospheres. The relationship is based on (1) permeability test data published by Whiting [17] and (2) relationships between intrinsic gas permeability and water permeability of near-surface concrete as presented by Dhir et al. [16].

For comparison purposes, slip flow constants predicted by an expression proposed by Bamforth [15] are also shown in Fig. 1. The variability illustrated in Fig. 1 is indicative of the effects of differences in mixture composition and in sample preparation and testing techniques. In Whiting's tests [17], concrete samples were oven-dried before gas permeability testing, whereas in Bamforth's tests [15], the samples were air-dried. Oven drying is well known to cause microcracking that increases the permeability of the material being tested. In contrast, when air-drying techniques are used instead, it is very difficult to completely desaturate the test specimen (a step that is necessary in the determination of intrinsic gas permeability). Even a small amount of residual moisture can significantly decrease the gas permeability that is experimentally determined [18]. As Fig. 1 suggests, gas-phase slip flow constants corresponding to typical concrete mixtures are approximately bounded at the upper end by Eq. (5) and at the lower end by Bamforth's expression.

3.2. Relative permeability of concrete

A complete description of moisture flow inside heated concrete requires not only that the intrinsic permeabilities of the material to liquid and gas flow be adequately quantified (including slip flow effects), but also that the interaction between the two moisture phases also be represented [15,16,18]. Partially saturated concrete exposed to severe fire involves two distinct fluid phases (liquid water and gaseous steam) permeating simultaneously through the

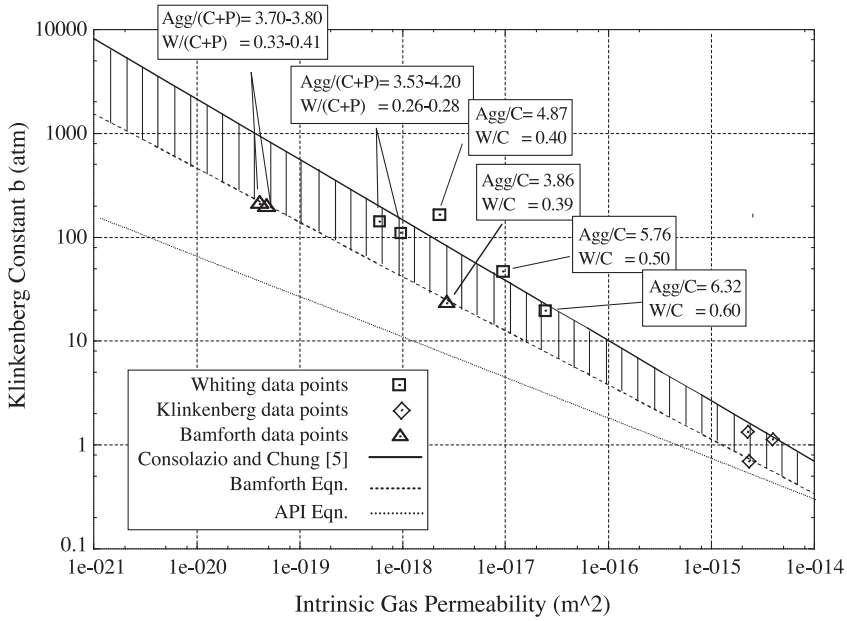

Fig. 1. Slip flow constant vs. the gas permeability of concrete.

porous network. The presence of the liquid phase reduces the permeability of the concrete to gas phase flow and vice versa. To model this phase-interference phenomenon mathematically, relative permeability functions are defined:

$$k_{\mathrm{rg}} = k_{\mathrm{rg}}(S_{\mathrm{g}}, n)$$

$$k_{\mathrm{rw}} = k_{\mathrm{rw}}(S_{\mathrm{w}}, n) \tag{6}$$

where $k_{r\pi}$ is the relative permeability of the concrete to phase π at the degree of fluid saturation S_{π}, and n is the concrete porosity. Both of the relative permeability functions obey the bounds $0 \le k_{r\pi}(S_{\pi}, n) \le 1$.

Employing the relationship $S_{\mathrm{g}} = 1 - S_{\mathrm{w}}$, the following k_{rg} function for cementitious materials has been developed [9]:

$$k_{\mathrm{rg}}(S_{\mathrm{w}}, \lambda) = 10^{S_{\mathrm{w}}\lambda} - 10^{\lambda} S_{\mathrm{w}} \tag{7}$$

where

$$\lambda = 0.05 - 22.5n \tag{8}$$

The expressions above quantify the reduction of gas permeability that occurs when liquid pore moisture is present (quantified by the liquid water saturation level S_{w}). These expressions have been developed by making

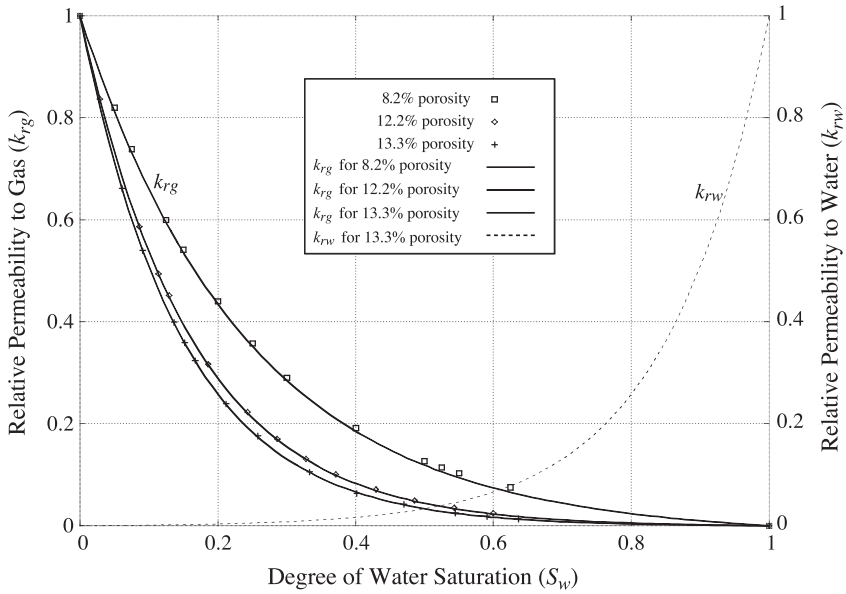

Fig. 2. Relative permeability functions for the gas phase.

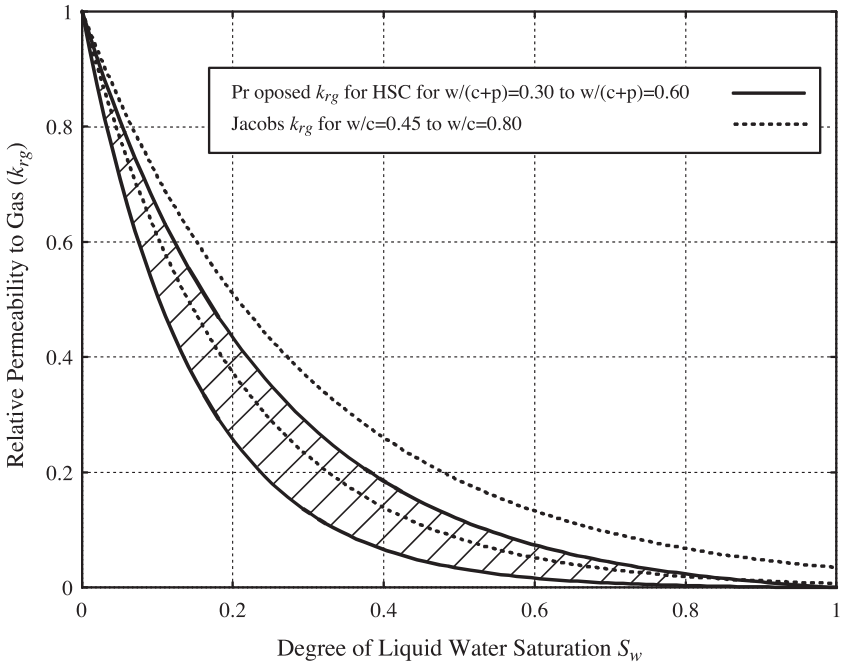

Fig. 3. Comparison of relative permeability functions for gas flow.

use of gas permeability test data [12,17,21,22] and sorption isotherm data [23] collected from the literature.

In terms of formulating a corresponding function k_{rw} for the liquid water phase, studies focusing on two-phase flow (air–water) and three-phase flow (air–water–oil) in soils were reviewed (e.g., Refs. [24–26]). A remarkable resemblance in the $k_{r\pi}$-saturation relations in two-phase (air–water) and three-phase (air–water–oil) flows is found in both shape and variation with respect to water saturation. Based on the results of this review, it was determined that a simple mirroring and scaling of the k_{rg} curve provides a rudimentary approximation of liquid-phase relative permeability:

$$k_{rw}(S_w) = k_{rg}(1 - S_w) \tag{9}$$

Significant refinement in the accuracy of the proposed k_{rw} function is not warranted in the current context because thermally driven moisture flow through concrete primarily involves gas phase fluid flow; thus the k_{rg} function is far more influential and important than the k_{rw} function.

Relative gas permeability curves generated by the k_{rg} function given above are plotted for various concrete porosity values in Fig. 2. In Fig. 3, a comparison between Eq. (7) and experimental results presented by Jacobs [27] is given. By conducting gas permeability tests on concrete specimens at various states of partial liquid saturation, Jacobs determined relative permeability values for gas flow (values of k_{rg} as a function of S_w). Upper and lower bound curves for Jacob's results for concrete specimens that had water to cement ratios (W/C) ranging approximately from 0.45 to 0.8, are shown in Fig. 3. For comparison, the range of values predicted by Eq. (7) for concrete mixes having W/(C + P) ranging approximately from 0.3 to 0.6, is also shown as a hatched region in Fig. 3. Although the two sets of curves are not identical, their general form is in good agreement. Because Eq. (7) has been developed using experimental data [16,17,21] separate from Jacobs' data, the agreement shown in Fig. 3 suggests a degree of validity in the relationships presented both here and by Jacobs [27].

4. Calculation of initial conditions

Initial conditions for the fire-exposure simulations presented here are assumed to be uniform conditions of pressure, temperature, and saturation throughout the entire domain. Initial pressure is assumed to be equal to standard atmospheric pressure and initial temperature is assumed to be 20 °C. Initial moisture contents for the partially saturated concrete mixtures considered here (Table 1) are computed using sorption isotherm data [22]. Using the porosity,

Table 1
Concrete material properties

Material property	Symbol	Concrete I (low permeability)	Concrete II (high permeability)
Initial saturation	S_w	0.4	0.3
Intrinsic gas permeability	K_g	2.24E − 17 m^2	2.17E − 15 m^2
Intrinsic liquid permeability	K_l	8.49E − 19 m^2	9.82E − 17 m^2
Slip–flow constant	b_{sf}	2.44 MPa	0.17 MPa
Porosity	n	13.3%	18.8%
Dry conductivity	κ_{dry}	1.7 W/m K	1.7 W/m K
Wet conductivity	κ_{wet}	2.9 W/m K	2.9 W/m K
Emissivity	ε	0.8	0.8
Specific heat	C_p	921.1 J/kg K	921.1 J/kg K

W/(C + P), Agg/(C + P), and saturated unit weight of the concrete, the total capillary water content of the concrete in the saturated condition is computed. This quantity is then converted into an equivalent "water content by mass of dried hardened cement paste (HCP) contained in the concrete (from mix proportions)" [22]. Thus, the "normal" mass water content is converted into one that is referenced only with respect to the portion of the concrete mass attributable to the cement paste. Using the sorption isotherms reported by Baroghel-Bouny and Chaussadent [22], moisture contents for two different types of concrete at ambient environmental conditions are then computed using the following procedure.

At two extremes are the fully saturated condition ($S_w = 1.0$) and the fully desaturated condition ($S_w = 0.0$). In partially saturated conditions between these two extremes, S_w is computed as a percentage of the saturated moisture content:

$$S_w = \frac{w_{rh;hcp}}{w_{sat;hcp}} \tag{10}$$

where $w_{sat;hcp}$ = water content (per unit weight of "dry" HCP) contained in concrete in a saturated condition and $w_{rh;hcp}$ = water content when the concrete is air-dried at a particular relative humidity level.

(a) Pore pressures measured experimentally and predicted using a 2-D simulation model

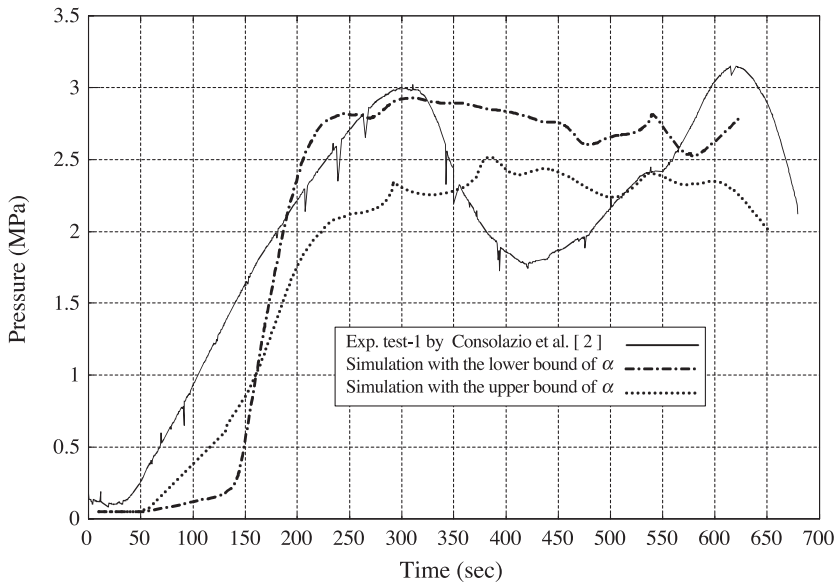

(b) Temperatures measured experimentally and predicted using a 2-D simulation model

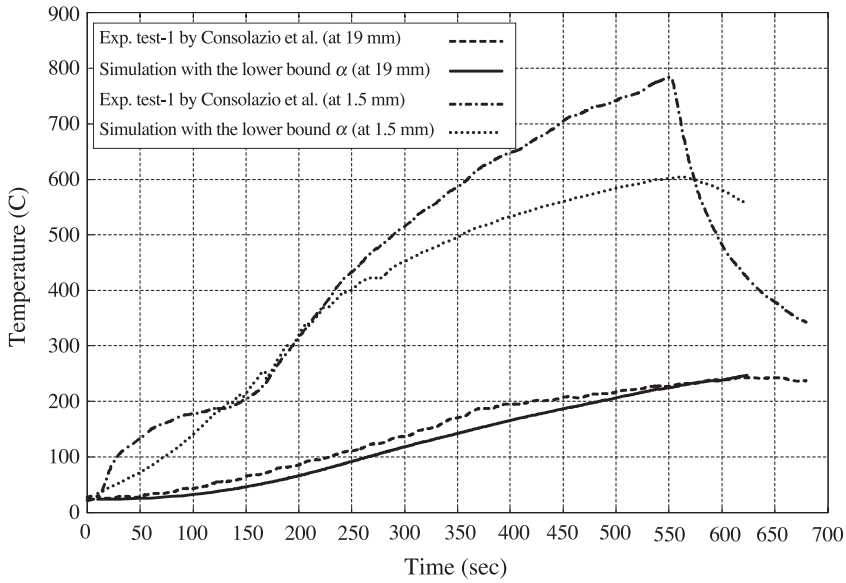

Fig. 4. Comparison of numerical prediction to experimental measurement.

To illustrate the process of initial saturation level determination, consider a concrete sample made of the low-permeability concrete [28] in Table 1 having porosity 0.133 (13.3%), W/(C + P) = 0.48, and Agg/(C + P) = 4.56. If the saturated unit weight of the concrete sample is 2400 kg/m^3 (150 lbs/ft^3), then the unit weight of "dry" HCP contained in the concrete may be approximated as 2400/(0.48 + 4.56 + 1.0) = 397.4 kg/m^3 (24.83 lbs/ft^3). Thus, the fully saturated water content per unit weight of "dry" HCP is estimated as $w_{sat;hcp}$=(0.133 × 1000.0)/397.4 = 0.335 (33.5%). To compute $w_{rh;hcp}$ in Eq. (10) of a concrete member that has reached hygrothermal equilibrium in an ambient environmental condition, a particular relative humidity level needs to be selected. Considering a concrete member in hygrothermal equilibrium at 60% relative humidity $w_{rh;hcp}$ is computed as 13.4% using isotherm data reported by Baroghel-Bouny and Chaussadent [22]. Therefore, the initial degree of saturation for the concrete would then be computed as S_w = 13.4/33.5 = 0.4 [9].

When a low-porosity, low-permeability concrete structure undergoes drying, the degree of liquid water saturation ultimately reached at environmental hygrothermal equilibrium will be higher than that which would be reached in a higher porosity, higher permeability concrete structure in the same relative humidity environment. As a result, although low-permeability concrete mixtures typically have lower initial water contents [due to lower W/(C + P)] than do high-permeability mixtures, the equilibrium water saturation level (S_w) reached in the former type of material will be *greater* than that of the latter (Table 1). As previous studies have demonstrated [5], initial liquid saturation levels can significantly influence moisture movement and the development of internal temperatures and pore pressures within concrete elements exposed to fire. Additional details may be found in Refs. [9,29].

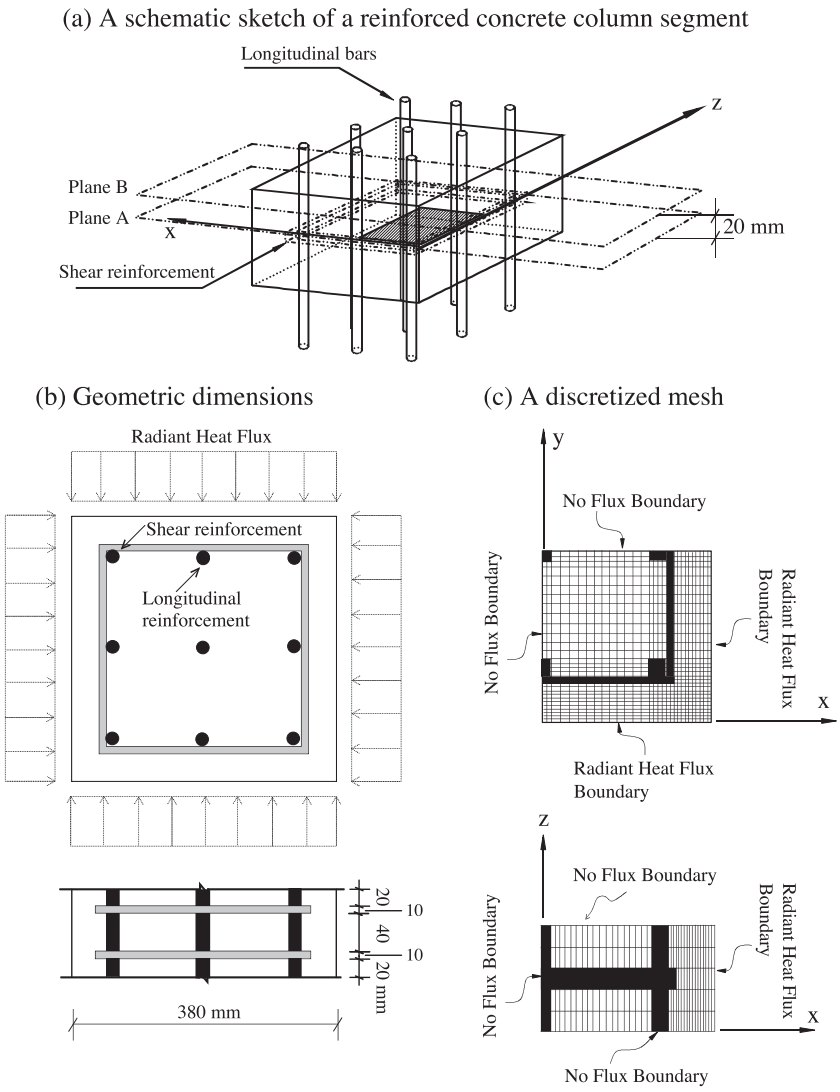

Fig. 5. Geometry of a 3-D simulation mesh and a thermal loading boundary.

5. Validation of proposed numerical model

Before conducting simulations of steel-reinforced concrete systems, the constitutive models proposed above are first validated against experimental data corresponding to thermal-exposure testing of saturated, but *unreinforced*, cementitious mortar specimens. A 2-D analysis is performed and results are compared to experimental data previously reported by the authors [2,5]. In the numerical analysis conducted here, both the slip–flow relationship expressed by Eq. (5) and the relative permeability relationships expressed by Eqs. (7) and (9) are used.

In the previous experimental studies [2], the intrinsic gas permeability and porosity of mortar specimens were experimentally determined to be $K_g = 8.3424\text{E}-16$ m^2 and $n = 14.5\%$, respectively; however, water permeability K_w was not measured. Therefore, in the present study, the water permeability of the mortar mixture is estimated indirectly. Because both aggregate type and Agg/(C + P) are well known to affect the water permeability of cementitious materials, rather than computing a single K_w, instead both upper and lower bound values are determined and simulations are conducted at each bound.

At the upper bound, K_w is computed using a relationship between intrinsic liquid and intrinsic gas permeability that is based on experimental data published by Dhir et al. [16]. Using the K_g value cited above and the data published by Dhir et al., upper bound water permeability values for the mortar in question is computed to be $K_w = 5.6728\text{E}-17$ m^2. If we define the ratio of intrinsic liquid permeability to intrinsic gas permeability as

$$\alpha = K_w / K_g \tag{11}$$

then α for the upper bound estimation of K_w would be $\alpha = 0.068$. A lower bound value is determined from water permeability data published by Whiting [17] for cementitious materials having porosities ranging from 7.5% to 14.7%. Interpolating Whiting's data at a porosity of 14.5%, lower bound water permeability values are computed to be $\alpha = 0.038$ and $K_w = 3.1701\text{E}-17$ m^2. Using both the upper and lower bound values, the thermal exposure conditions tested by Consolazio et al. [2] are numerically simulated using the constitutive and numerical analysis procedures described above. A comparison of numerical and experimental results are presented in Fig. 4.

In Fig. 4a, pore pressures occurring at a position 19 mm from the heated surface are compared to experimental data measured at the same location. Peak pore pressure predicted by the lower bound numerical simulation is shown to match well with the corresponding value measured experimentally.

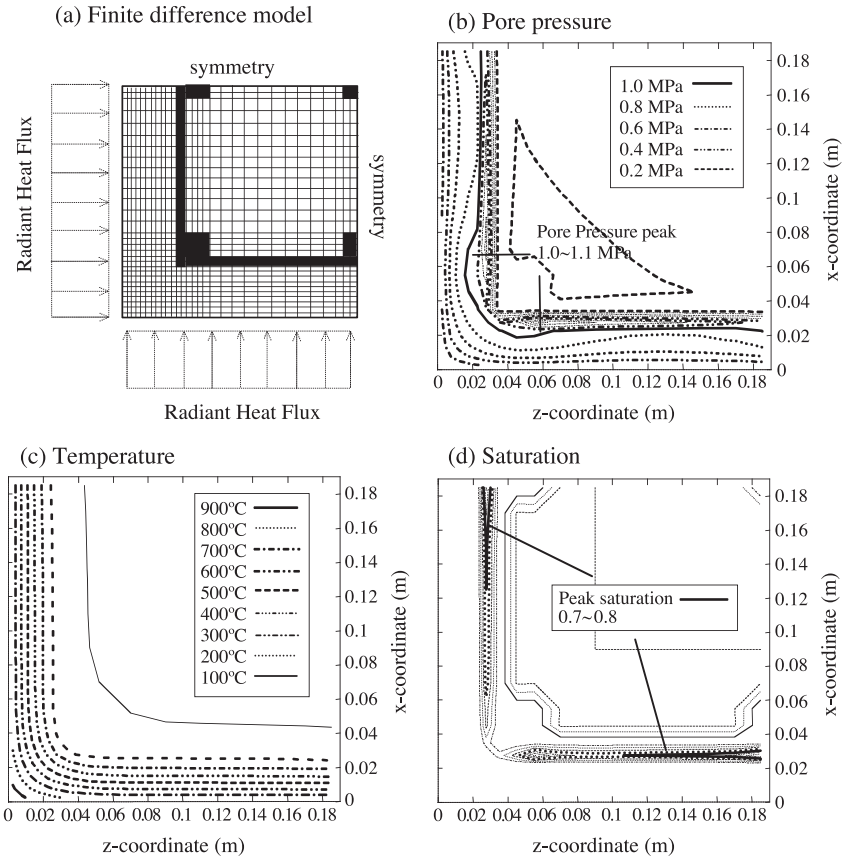

Fig. 6. Thermodynamic states of a high-permeability concrete at $t = 600$ s (data plotted for a square column segment Plane A of Fig. 5).

It is necessary to note that the pore pressure dip in the experimental case was found [2] to be attributable to small voids created when placing pore pressure transducers within the mortar specimens. Thus, the pressure dip is the product only of the specific instrument setup used and is not a phenomenon that would normally occur in a noninstrumented specimen [2] as has been numerically simulated here. As such, it is not of concern in terms of validating the present numeric model.

In Fig. 4b, comparisons are provided between temperatures measured experimentally and corresponding values predicted numerically (using the lower bound α). Immediately adjacent to the heated surface (at a depth of 1.5 mm), the agreement is reasonable but differences are observed. At such a close position to the heated surface, the temperature gradient is extremely steep. As a result, even minor differences in temperature sampling location will yield significantly different predicted and measured temperatures. Also, the precise mode of surface heating (mixture of radiation and convection) will also influence internal temperature development. At 19 mm from the heated surface, where surface effects are less influential, predicted and measured temperatures are in good agreement, indicating that conductive and convective heat transfer within the specimen is properly modeled.

6. Numerical simulation of concrete with steel reinforcement

Focus is now turned to studying the effects of reinforcing steel on moisture movement in R/C structures exposed to fire. To study moisture flow through heated R/C, a 3-D simulation model is constructed that includes concrete and both longitudinal and shear reinforcement (Fig. 5). The model represents a 0.38×0.38 m reinforced concrete column. Columns consisting of two different types of concrete (Table 1) are simulated. The influence of the steel reinforcement on hydrothermal behavior is investigated and the effects of low permeability on the development of thermodynamic profiles are quantified.

6.1. Modeling initial and boundary conditions

In each simulation conducted, uniform initial conditions are assumed. Initial pressure and temperature are 0.1013 MPa (1 atm) and 20 °C, respectively. Initial liquid saturation levels are $S_w = 0.4$ for Concrete I (low-permeability concrete) and $S_w = 0.3$ for Concrete II (high-permeability concrete), each of these values corresponding to hygrothermal equilibrium at 60% relative humidity in an ambient temperature of 20 °C. Due to symmetry of the column

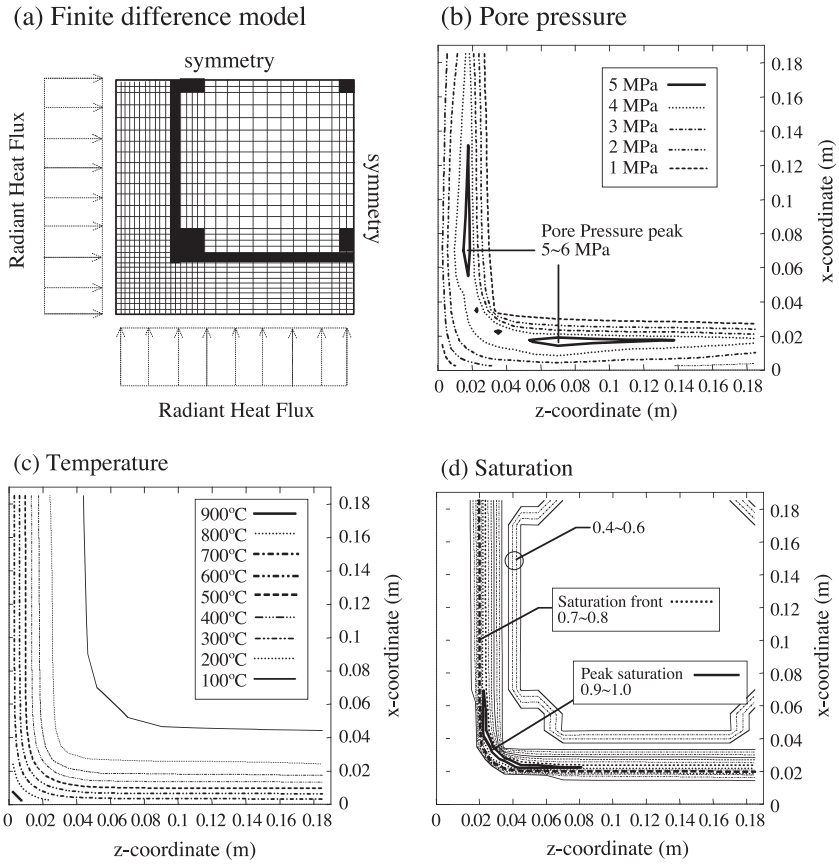

Fig. 7. Thermodynamic states of a low-permeability concrete at $t = 600$ s (data plotted for a square column segment Plane A of Fig. 5).

cross-sectional geometry and symmetry of the thermal loading, partial models (Fig. 5) with zero-flux boundary conditions at the symmetric surfaces are used. For each radiant heat flux boundary, denoted Γ_q, the heat source is modeled as:

$$-\kappa\frac{\partial T}{\partial n} = T(t) \text{ on } \Gamma_q \tag{12}$$

where κ represents the thermal conductivity of the boundary between the radiant heat source and the exposed surface and n represents the surface normal to the boundary Γ_q. Surface heat fluxes due to the fire and moisture flow from the column to the surrounding atmosphere are modeled using procedures previously described [2,30] and therefore are not detailed here.

6.2. Simulation results

Moisture transport phenomena associated with heating during the first 5 min of fire exposure (modeled using ASTM E1529 [31]) are found to have nearly negligible effects on the development of pore pressures in both cases of Concrete I and II. After 10 min of fire exposure, pore pressures in the high-permeability, low-initial-saturation case (Concrete II) are found to be relatively small (Fig. 6). However, at the same point in time, the low-permeability, high-initial-saturation case (Concrete I) reveals that steel reinforcing has a significant influence on transport phenomena and the evolution of temperature, pressure, and saturation.

Figs. 7 and 8 illustrate the thermodynamic field variables developed at two different locations in the column made of Concrete I at $t=600$ s. Numerically computed volume-averaged pore pressures in the plane where shear reinforcement is located (Fig. 7a) reach 5.5 MPa (0.8 ksi) at time $t=600$ s. Interestingly, the development of peak pore pressure is predicted along the interface between the concrete and shear reinforcement parallel to the surfaces exposed to the fire. Similar trends of pore pressure are found in the plane located 20 mm vertically above the shear reinforcement, i.e., Plane B of Fig. 5a. In the corner region of the square column, the maximum value of volume-averaged pore pressure that occurs in Plane B exceeds 6.7 MPa (0.97 ksi) at time $t=600$ s. Unexpectedly, as heating continues, the pore pressures that develop in the region between the shear ties (Plane B) exceed those that develop adjacent to the shear ties (Plane A).

Steel shear reinforcement effectively blocks horizontal moisture flow in the xz plane and forces moisture to permeate vertically around the rebar and in a direction parallel to the column surface. Comparing Fig. 7d to Fig. 8d, more prominent development of moisture clogging

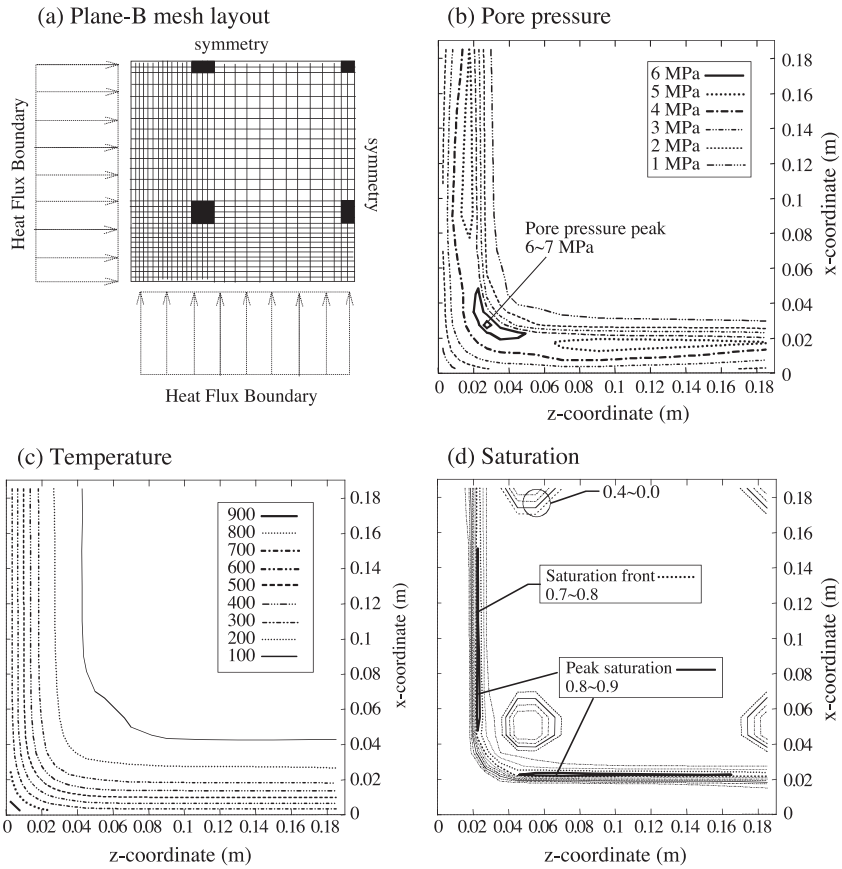

Fig. 8. Thermodynamic states of a low-permeability concrete at $t=600$ s (data plotted for a square column segment Plane B of Fig. 5).

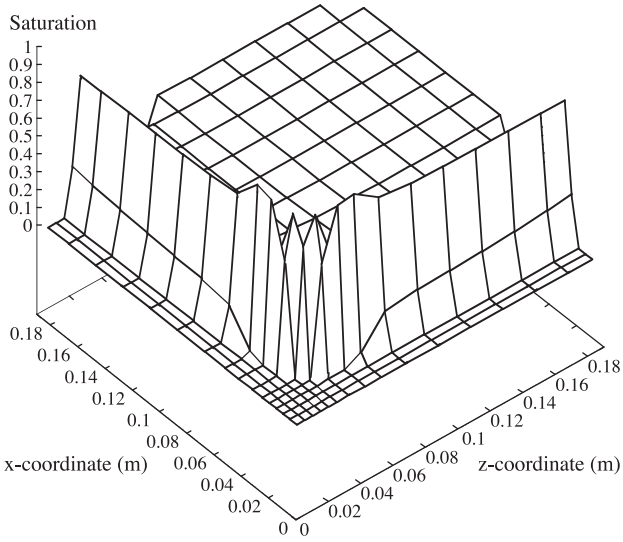

Fig. 9. Moisture clog formed in a square column.

(accumulation of liquid saturation) is observed in Fig. 7d than in Fig. 8d. This is a clear indication that the shear steel is blocking the flow of moisture. In addition, the influence of saturation formation on pore pressure development is evident in Figs. 7d and 8d. Locations of maximum pore pressure are found to be within two-phase zones (liquid/vapor mixture) adjacent to the locations at which the liquid saturation maximizes [32].

It is noteworthy that the water saturation level in a large portion of the section is nearly at the maximum theoretical value of unity. As a result, a nearly impermeable "wall" of liquid moisture is formed (Fig. 9). This zone acts as a thermal barrier (heat sink) in that the moisture consumes a large amount of thermal energy during the evaporation process and thus reduces the flow of heat into the substrate concrete. This in turn limits the rate of temperature rise in the concrete and retards the development of thermal stresses. A high level of pore water content is thus beneficial for effectively protecting surface concrete from fire at later stages of heating, but the same moisture leads to the development of significant pore pressures during moisture vaporization in the heating process.

7. Conclusion

Temperature, saturation, and pore pressure distributions have been investigated in connection to the development of thermodynamic states in reinforced concrete elements exposed to fire. The numerical model presented here accounts for three important phenomena involved in heat transfer: (1) interference between the liquid and gas phases, (2) slip flow effects in steam flow, and (3) moisture clogging due to presence of the steel reinforcement. The effects of steel reinforcement on heat and mass transfer in the surface region of an R/C column are found to influence moisture clog formation as well as temperature and pressure development.

Simulations presented here predict that the presence of steel reinforcement impedes moisture movement and produces quasi-saturated moisture-clog zones that lead to the development of significant pore pressures. In addition, these zones alter the flow of heat into the system and tend to attenuate the rise of internal temperature. It is therefore evident that thermally induced stresses in cover concrete are related not only to the external thermal loading, but also to moisture flow, reinforcing steel placement, and thermal processes such as evaporation [5,33]. The model presented here offers an improved tool for studying multidimensional thermodynamic state evolution inside reinforced concrete structural elements subjected to severe fire exposure. In addition, it serves as a basis for developing improved flow models. For example, one factor influencing pore pressure that is beyond the scope of this paper is the increase of concrete permeability at high temperatures [4,34]. Expansion of micropore volume and cracking induced by shrinkage (due to dehydration of cement gels at high temperatures) are phenomena that can increase the permeability of concrete. In the future, an enhanced flow model incorporating such effects may be implemented once additional experimental data become available.

Nomenclature

n porosity
S degree of saturation
C_p specific heat
K intrinsic permeability
$k_{r\pi}$ relative permeability function of fluid phase
P pressure
b Klinkenberg's constant
T absolute temperature
H latent heat
v macroscopic mean velocity
x coordinate axis

Greek symbols

π phase
ρ density
μ dynamic viscosity
τ tortuosity
κ^{π} thermal conductivity of phase π
κ_{eff} effective thermal conductivity
η volume fraction
α,λ parameters used in relative permeability function
Γ boundary
Ω total flow domain

Subscripts and superscripts

w liquid water phase
g gas phase
s solid phase

Acknowledgements

The authors wish to acknowledge the financial support of the National Science Foundation under Grant No. CMS-9900015.

References

[1] V.K.R. Kodur, Studies on the fire resistance of high-strength concrete at the National Research Council of Canada, International Workshop on Fire Performance of High-Strength Concrete, NIST Special Publication, vol. 919, National Institute of Standards and Technology, Gaithersburg, MD, 1997, pp. 75–86.
[2] G.R. Consolazio, M.C. McVay, J.W. Rish III, Measurement and prediction of pore pressures in saturated cement mortar subjected to radiant heating, ACI Mater. J. 95 (5) (1998) 526–536.
[3] V.K.R. Kodur, Fire performance of high-strength concrete structural members, Construction Technology Update, vol. 31, National Research Council of Canada, Ottawa, Canada, 1999.
[4] L.T. Phan, N.J. Carino, Review of mechanical properties of HSC at elevated temperature, J. Mater. Civ. Eng. 10 (1) (1998) 58–64.
[5] G.R. Consolazio, J.H. Chung, Numeric simulation of near-surface moisture migration and stress development in concrete exposed to fire, Comput. Concr. 1 (1) (2003) 31–46.
[6] S.Y.N. Chan, G.F. Peng, M. Anson, Fire behavior of high-performance concrete made with silica fume at various moisture contents, ACI Mater. J. 96 (3) (1999) 405–409.
[7] P. Kalifa, F.D. Menneteau, D. Quenard, Spalling and pore pressure in HPC at high temperature, Cem. Concr. Res. 30 (12) (2000) 1915–1927.
[8] K. Pruess, TOUGH2: A General-Purpose Numerical Simulator for Multiphase Fluid and Heat Flow, Document LBL-29400, Earth Sciences Division, Lawrence Berkeley Laboratory, University of California, Berkeley, CA, 1991.
[9] J.H. Chung, Numerical simulation of hydro–thermo–mechanical behavior of concrete structures exposed to elevated temperatures, Doctoral dissertation, Department of Civil and Coastal Engineering, University of Florida, 2003.
[10] B.B. Hope, V.M. Malhotra, The measurement of concrete permeability, Can. J. Civ. Eng. 2 (3) (1984) 287–292.
[11] S. Nagataki, I. Ujike, N. Konishi, Influence of moisture content on air permeability of concrete, Review of 40 Meeting of Cement Association of Japan, Tokyo, Japan Concrete Institute, Tokyo, Japan, 1986, pp. 158–161.
[12] M.C. McVay, J.W. Rish III, Flow of nitrogen and superheated steam through cement mortar, J. Thermophys. Heat Transf. 9 (4) (1995) 790–792.
[13] H.W. Reinhardt, A. Dinku, Effects of curing on the gas permeability of cover concrete, in: H. Jennings, K. Scrivener, J. Kropp (Eds.), The Modeling of Microstructure and Its Potential for Studying Transport Properties and Durability, Nato ASI Series vol. 304, Kluwer Academic Publishers, Boston, 1996, pp. 325–337.
[14] T. Sugiyama, T.W. Bremner, T.A. Holm, Effect of stress on gas permeability in concrete, ACI Mater. J. 93 (5) (1996) 443–450.
[15] P.B. Bamforth, The relationship between permeability coefficients for concrete obtained using liquid and gas, Mag. Concr. Res. 39 (138) (1987) 3–11.
[16] R.K. Dhir, P.C. Hewlett, Y.N. Chan, Near surface characteristics of concrete: intrinsic permeability, Mag. Concr. Res. 41 (147) (1989) 87–97.
[17] D. Whiting, Permeability of selected concrete, in: D. Whiting, A. Walitt (Eds.), Permeability of Concrete, ACI SP-108, American Concrete Institute, Detroit, MI, USA, 1988, pp. 195–222.
[18] K. Li, R.N. Horne, Gas slippage in two-phase flow and the effect of temperature, SPE 68778, Society of Petroleum Engineers, presented at the 2001 SPE Western Region Meeting, SPE, P.O. Box 833836, Richardson, TX 75083-3836.
[19] L.T. Phan, N.J. Carino, Effects of test conditions and mixture proportions on behavior of high-strength concrete exposed to high temperatures, ACI Mater. J. 99 (1) (2002) 54–66.
[20] L.J. Klinkenberg, The permeability of porous media to liquids and gases, Drilling and Production Practice, American Petroleum Institute, Washington DC, USA, 1941, pp. 200–207.
[21] J.G. Cabrera, P. Ghoddoussi, The influence of fly ash on the resistivity and rate of corrosion of reinforced concrete, in: V.M. Malhotra (Ed.), Durability of Concrete, ACI SP-145, American Concrete Institute, Detroit, MI, USA, 1994, pp. 229–244.
[22] V. Baroghel-Bouny, T. Chaussadent, Texture and moisture characterization of hardened cement pastes and concrete from water vapor sorption measurements, in: H. Jennings, K. Scrivener, J. Kropp (Eds.), The Modeling of Microstructure and Its Potential for Studying Transport Properties and Durability, Nato ASI Series vol. 304, Kluwer Academic Publishers, Boston, 1996, pp. 241–255.
[23] K.K Hansen, Sorption isotherms: a catalog and a data base, ASTM STP 1039, Water Vapor Transmission Through Building Materials and Systems, American Society for Testing and Materials, West Conshohocken, PA, 1989, pp. 28–32.
[24] R.J. Lenhard, J.C. Parker, A model for hysteretic constitute relations governing multiphase flow 2. Permeability–saturation relations, Water Resour. Res. 12 (2) (1987) 2197–2206.
[25] N.T. Burdine, Relative permeability calculations from pore-size distribution data, Pet. Trans. AIME 198 (1953) 71–77.
[26] J.C. Parker, R.J. Lenhard, T. Kuppusamy, A parametric model for constitutive properties governing multiphase flow in porous media, Water Resour. Res. 23 (4) (1987) 618–624.
[27] F. Jacobs, Permeability to gas of partially saturated concrete, Mag. Concr. Res. 50 (2)Portland Cement Association, Skokie, IL, 1998 (1998) 115–121.
[28] R.G. Burg, B.W. Ost, Engineering properties of commercially available high strength concretes (including three year data), PCA Research and Development Bulletin RD104T, Portland Cement Association, Skokie, IL, 1994.
[29] D. Gawin, C.E. Majorana, B.A. Schrefler, Numerical analysis of hygro-thermal behavior and damage of concrete at high temperature, Mech. Cohes.-Frict. Mater. 4 (1999) 37–74.
[30] S.V. Patankar, Numerical Heat Transfer and Fluid Flow, Taylor and Francis, New York, NY, 1980.
[31] STM E1529-93, Standard test methods for determining effects of large hydrocarbon pool fires on structural members and assemblies, Annual Book of ASTM Standards, American Society for Testing and Materials, West Conshohocken, PA, USA, 1993, pp. 688–701.
[32] K. Preuss, C. Calore, R. Celati, Y.S. Wu, An analytical solution for heat transfer at a boiling front moving through a porous medium, Int. J. Heat Mass Transfer 30 (12) (1987) 2595–2602.
[33] G. Sanjayan, L.G. Stocks, Spalling of high-strength silica fume concrete in fire, ACI Mater. J. 90 (2) (1993) 170–173.
[34] I. Janotka, L. Bágel, Pore structures, permeabilities, and compressive strengths of concrete at temperatures up to 800 °C, ACI Mater. J. 99 (2) (2002) 196–200.